

We are IntechOpen, the world's leading publisher of Open Access books Built by scientists, for scientists

6,900

Open access books available

186,000

International authors and editors

200M

Downloads

Our authors are among the

154

Countries delivered to

TOP 1%

most cited scientists

12.2%

Contributors from top 500 universities



WEB OF SCIENCE™

Selection of our books indexed in the Book Citation Index
in Web of Science™ Core Collection (BKCI)

Interested in publishing with us?
Contact book.department@intechopen.com

Numbers displayed above are based on latest data collected.
For more information visit www.intechopen.com



Grazing Incidence Small Angle X-Ray Scattering as a Tool for In-Situ Time-Resolved Studies

Gonzalo Santoro and Shun Yu

Additional information is available at the end of the chapter

<http://dx.doi.org/10.5772/64877>

Abstract

With the advent of third-generation synchrotron sources and the development of fast two-dimensional X-ray detectors, X-ray scattering has become an invaluable tool for in-situ time-resolved experiments. In the case of thin films, grazing incidence small angle X-ray scattering (GISAXS) constitutes a powerful technique to extract morphological information not only of the thin film surface but also of buried structures with statistical relevance. Thus, recently in-situ GISAXS experiments with subsecond time resolution have enabled investigating the self-assembly processes during vacuum deposition of metallic and organic thin films as well as the structural changes of polymer and colloidal thin films in the course of wet deposition. Moreover, processing of thin films has also been investigated in-situ employing GISAXS. In this chapter, we review the current trends of time-resolved GISAXS studies. After an introduction to the GISAXS technique, we present exemplary results of metallic and organic thin film preparation, wet deposition of polymer thin films and self-assembly of colloidal thin films, as well as examples of thin film modification in, e.g., microfluidic channels and within working devices. Finally, an overview of the future perspectives in the field is provided.

Keywords: GISAXS, thin films, time-resolved experiments, kinetics, processing

1. Introduction

Nanostructures have become commonly used in our daily lives because of the novel properties arising at the nanoscale. These are mainly associated to the object size offering a higher surface-to-volume ratio than macroscopic entities and, thus, surface processes become more

and more crucial as the material size is reduced. Furthermore, during the last half century several ways of manipulating the materials at the nanometer scale have been developed to control the nanostructure morphology on demand via either building up the nanostructures by atomic manipulation or exploiting self-assembly concepts. The latter presents clear advantages over atomic manipulation such as less demanding fabrication steps and easier scale-up for industrial production. Nevertheless, much is yet to be understood concerning self-assembly. In this sense, apart from the manipulation of materials at the nanoscale, an appropriate and accurate characterization of nanostructures is crucial, especially for studying the kinetics both during fabrication and processing of the nanostructures.

To properly characterize nanostructures, two questions need to bear in mind: what is the size/shape of the nanostructure and how do they separate from each other. The former is critical since nanostructure geometry strongly influences, e.g., the geometric confinement of the electronic structure [1], the catalytic activity [2, 3] or the optical properties [4, 5]. The latter is important since different physical properties may arise from particular nanostructure arrangement or in the space confined between the nanostructures, e.g., highly ordered arrays of plasmonic nanostructures present a collective plasmonic behavior [6], an efficient arrangement of the nano-objects may expose higher surface area on a macroscopic level for catalysis applications [7] or polymers within nanostructured media may show different glass transition temperatures and chain mobility due to confinement [8].

Within a non ideal material system, the size of the nanostructures and the spatial arrangement present a distribution over micro/macroscale regions. Thus, the collective effects of nanostructured objects call for sound statistic evaluation. In this respect, grazing incidence small angle X-ray scattering (GISAXS) is nowadays one of the most interesting techniques for studying the morphology of nanostructured thin films. As its counterpart, transmission SAXS [9], it is sensitive to the size and shape of the nanoparticles and to the correlation distances between them, being capable of resolving objects and distances ranging from few nanometers to several hundreds of nanometers, in real space. In contrast to SAXS, GISAXS inherently presents high surface sensitivity as a consequence of the measurement geometry employed. In GISAXS, the incident X-ray beam impinges the sample at shallow angles, thus total external reflection on the surface may take place. In addition, this implies that the beam footprint on the sample probes macroscopic areas which, together with the nature of reciprocal space techniques, ensure that high sampling statistics is achieved.

GISAXS was first demonstrated by Levine et al. using a lab source [10]. However, the full potential of GISAXS is realized when a synchrotron is used as X-ray source. This is due to several reasons. First, a high photon flux is required to probe the surface structures, which may be only present in small amount in comparison to the bulk substrate, thus presenting a weak scattering signal; second, highly collimated beams are demanded to improve the reciprocal space resolution, thus the low emittance, small divergence, and partially coherent beams provided by synchrotron radiation sources are in great favor; third, synchrotron sources provide tunable X-ray wavelength, which may be used to probe the chemical composition in parallel to exploring the morphology.

The high X-ray photon flux of synchrotron sources extremely diminishes the acquisition time of a GISAXS pattern. This fact, along with a high flexibility in sample environments—e.g., vacuum chambers, liquid cells, heating stages, vapor exposure chambers, etc.—makes GISAXS a very powerful tool for acquiring morphological information on kinetic processes, which is extremely relevant to elucidate self-assembly processes. Additionally, the combination of parallel characterization techniques—e.g., optical spectroscopy and microscopy, electrical and magnetic characterization—allows correlating the structural information to the properties of the thin films, of utmost importance for tailoring the thin film functionality.

However, to carry out in-situ GISAXS, the high quality X-ray beam offered by synchrotron sources is not sufficient. The development of the 2D pixel detector, especially single photon counter, has played an important role. The high quantum efficiency and fast read-out time of 2D photon-counting pixel detectors can be translated to lower acquisition times—in comparison with CCD detectors; however, at present, CCD cameras offer small pixel size, implying higher resolution in reciprocal space. The low acquisition time renders a faster capture of the morphological features and the fast detector read-out time and efficiency enable high acquisition rates, thus it is possible to promptly track morphological development and/or modifications.

In this chapter, we will present the current trends of in-situ time-resolved GISAXS investigations during thin film preparation and processing. The chapter is structured as follows. Section 2 briefly introduces the GISAXS theory and analysis of GISAXS patterns. In Section 3, selected examples of in-situ GISAXS studies during the vacuum deposition of metals and organic thin films, as well as in-situ GISAXS investigations of wet deposition processes, are presented. Some exemplary studies of thin film processing and in-operando devices in which the use of in-situ GISAXS has resulted essential are compiled in Section 4. Finally, the conclusions and future perspectives of the field, according to the authors' opinion, are summarized in Section 5.

2. Grazing incidence small angle X-ray scattering

In this section, the basics of GISAXS will be shortly described. For more detailed information on the GISAXS theory, the readers are referred to [11–13].

2.1. Geometry, index of refraction and penetration depth

The main particularity of GISAXS lies on the geometry employed. Whereas in SAXS a transmission geometry is used, in GISAXS the X-ray beam impinges on the sample surface under a shallow incident angle, α_i , typically of tenths of a degree. The intensity scattered by the sample is then collected with a two-dimensional (2D) detector as a function of the exit, α_f , and out-of-plane, ψ , angles being the scattering plane that defined by the incident and specularly reflected X-rays. Typical sample-to-detector distances are in the range of 2–5 m and typical values of the scattering vector modulus q are 1–0.01 nm⁻¹, i.e., structures in the range of one to several hundred nanometer size in real space are probed by GISAXS.

The coordinate system usually selected in GISAXS presents the x -axis in the direction of the X-ray beam, the y -axis parallel to the sample surface and the z -axis along the surface normal.¹ The scattering geometry is depicted in **Figure 1**.

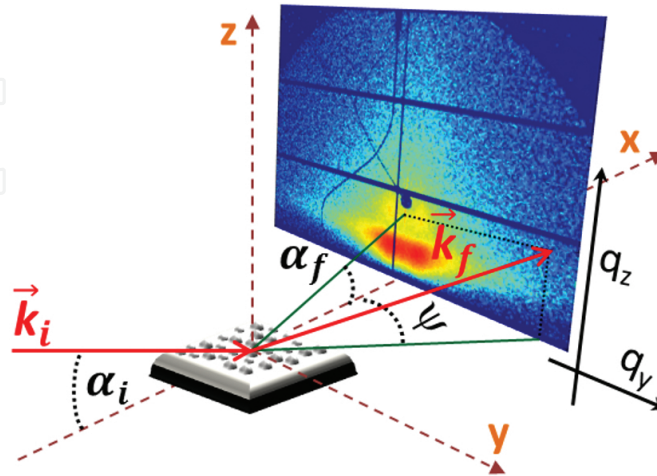


Figure 1. Sketch of the GISAXS scattering geometry. The sample is inclined by a small angle α_i with respect to the incoming X-ray beam and the diffuse scattering is recorded using a 2D detector as a function of the exit angles α_f and ψ . Typical sample-to-detector distances range from 2 to 5 m. Experimentally, the specular and the direct X-ray beams are commonly blocked by beamstops (the specular beamstop is the dark blue circle in the GISAXS pattern shown whereas the direct beamstop is not shown) to prevent the detector from oversaturation due to its strong intensity.

Within this coordinate system, the scattering vector, \vec{q} , i.e., the wave vector transfer due to the scattering event, in the case of monochromatic X-rays with an incident wave vector \vec{k}_i and wave number $k_0 = 2\pi/\lambda$ scattered along the \vec{k}_f direction is given by

$$\vec{q} = \vec{k}_f - \vec{k}_i = \begin{pmatrix} q_x \\ q_y \\ q_z \end{pmatrix} = \frac{2\pi}{\lambda} \begin{pmatrix} \cos(\alpha_f)\cos(\psi) - \cos(\alpha_i) \\ \cos(\alpha_f)\sin(\psi) \\ \sin(\alpha_i) + \sin(\alpha_f) \end{pmatrix} \quad (1)$$

Due to the small incident and exit angles involved in the GISAXS geometry a description of the sample based on a mean refractive index is sufficient and basically scattering arises from the variations in refractive index²

¹ For reasons out of our knowledge, the axes of the coordinate system commonly employed, and more often found in the literature, form an inverse trihedral angle—i.e., the axes are defined by the vector product $\hat{x} \times \hat{y} = -\hat{z}$, where, \hat{x} , \hat{y} and \hat{z} represent the axis unit vectors—instead of the usual direct trihedral angle. Anyway, since all the angles involved in GISAXS geometry are small, q_x is negligible (Eq. (1)) and this axis selection is not particularly relevant.

² Strictly, the responsible for the scattering events is the variation in electron density, which in a simplified manner is taken into account using a mean refractive index.

$$n(\lambda) = 1 - \delta(\lambda) + i\beta(\lambda) \quad (2)$$

where $\delta(\lambda)$ and $\beta(\lambda)$ represent the dispersion and absorption parts of X-rays, respectively, and are given by the following expressions:

$$\delta(\lambda) = \frac{r_e \lambda^2}{2\pi} \rho \frac{\sum_k [f_k^0(\lambda) + f'_k(\lambda)]}{\sum_k M_k} \quad (3)$$

$$\beta(\lambda) = \frac{r_e \lambda^2}{2\pi} \rho \frac{\sum_k f''_k(\lambda)}{\sum_k M_k} \quad (4)$$

in which $r_e = e^2/4\pi\epsilon_0 m_e c^2$ is the classical electron radius, λ the wavelength, ρ the material mass density and M_k the atomic mass. f_k^0 is the nonresonant term of the atomic scattering factor and can be approximated by the number of electrons Z_k whereas f'_k and f''_k are the dispersion corrections. The summations are performed over all k atoms within the unit cell, molecule or, in the case of polymers, repeating unit.

Since diffuse scattering can be ascribed to changes in the refractive index any type of surface roughness or electronic contrast variation gives rise to diffuse scattering which contains the morphological information of the probed film.

On the other hand, in the case of X-rays the refractive index is less than unity, implying that total external reflection takes place for angles below the critical angle $\alpha_c(\lambda)$ of the material, which is given by

$$\alpha_c = \sqrt{2\delta} \quad (5)$$

The diffuse scattering at $\alpha_{i,f} = \alpha_c$ presents a maximum that is referred to as the Yoneda peak [14] and its position is dependent on the material³, as is evident from Eqs. (3) and (5). The X-ray penetration depth varies from several nanometers, for incident angles below α_c , to several microns, for incident angles above α_c . In the ideal case of a perfectly flat film the penetration depth, Λ , defined as the depth at which the X-ray intensity is attenuated by $1/e$, for $\alpha_i, \alpha_c \ll 1$ and $\alpha_i = \alpha_f$ adopts the following expression⁴ [16, 17]:

³ Experimentally, the Yoneda peak is found at $\alpha_y = \alpha_i + \alpha_c$ with respect to the direct beam on the detector, since it is the sample which is tilted whereas the incoming X-ray beam remains normal to the detector plane. At an angle α_i from the direct beam position the so-called sample horizon is found and the scattering below the sample horizon is mainly due to scattering through the sample, i.e., in transmission geometry, especially for angles well above the critical angle of the probed film. See [15].

⁴ Actually, the depth probed in GISAXS depends on both the incident and exit angles since it is defined as the inverse of the imaginary part of q_z that presents a dependence on both angles. The probed depth is a combination of the penetration depth—incoming beam—and the depth from which scattering escapes the sample—exit beam. See [16, 17].

where β is the imaginary part of the refractive index. Thus, by varying the incident angle different film depths can be probed (**Figure 2**).

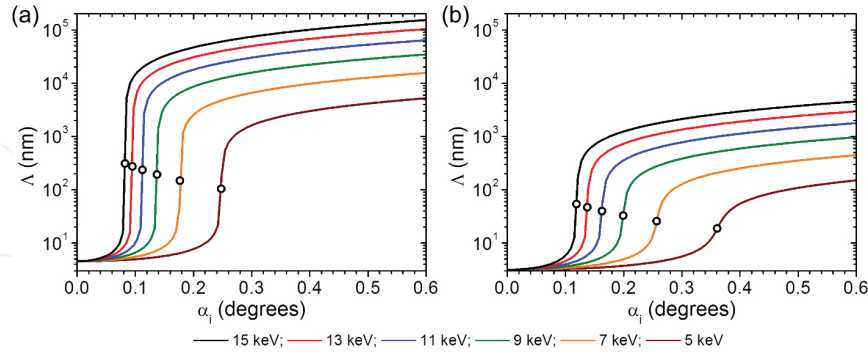


Figure 2. Penetration depth for $\alpha_i, \alpha_c \ll 1$ and α_i, α_c as a function of the incident angle at different X-ray energies for (a) polystyrene (PS) and (b) Si. In (a), a mass density of 1.04 g/cm^3 has been assumed. The dots represent the penetration depth at α_c for each energy.

$$\Lambda = \frac{\lambda}{4\pi} \sqrt{\frac{2}{\sqrt{(\alpha_i^2 - \alpha_c^2)^2 + 4\beta^2} - (\alpha_i^2 - \alpha_c^2)}} \quad (6)$$

From the scattering geometry alone, two major advantages of GISAXS over standard microscopic techniques are easily inferred. First, due to the small incident angle used, scattering comes from all the illuminated area within the X-ray footprint—in the order of several mm even for microfocus GISAXS (μ GISAXS), i.e., GISAXS performed with X-ray beam sizes of few tenths of microns or lower in both the horizontal and vertical directions—thus providing information of statistical relevance. Second, information not only from the surface but also from buried structures is accessible simply by tuning the incident angle of the X-ray beam with respect to the sample surface normal.

2.2. Scattering intensity: form factor and structure factor

The fact that GISAXS is performed at incident angles close to the critical angle implies that reflection on the surface can occur and thus multiple scattering effects take place. As a consequence the Born approximation (BA) is no longer valid and the diffuse scattering is typically analyzed within the framework of the distorted-wave Born approximation (DWBA) to account for reflection/refraction effects. Nevertheless, the basic concepts from the analysis of transmission scattering still apply, namely the use of a form factor and a structure factor. At present, several software packages are available for modeling of GISAXS data employing the DWBA [18–21].

In the simple BA, the form factor is the Fourier transform of the shape function of the scattering object

$$F(\vec{q}) = \int \exp(i\vec{q} \cdot \vec{r}) d^3r \quad (7)$$

In the DWBA, for the case of a simple object located on a solid substrate, this form factor is replaced by the coherent sum of four terms to take into account different scattering events that involve the reflection of the incident or scattered X-ray beam on the substrate.⁵ Thus, the form factor adopts the following expression

$$F_{DWBA}(\vec{q}_{\parallel}, q_z) = F(\vec{q}_{\parallel}, k_{z,f} - k_{z,i}) + R(\alpha_i)F(\vec{q}_{\parallel}, k_{z,f} + k_{z,i}) + R(\alpha_f)F(\vec{q}_{\parallel}, -k_{z,f} - k_{z,i}) + R(\alpha_i)R(\alpha_f)F(\vec{q}_{\parallel}, -k_{z,f} + k_{z,i}) \quad (8)$$

being $R(\alpha_i)$ and $R(\alpha_f)$ the Fresnel reflection coefficients of the substrate. These four terms are schematically represented in **Figure 3**.

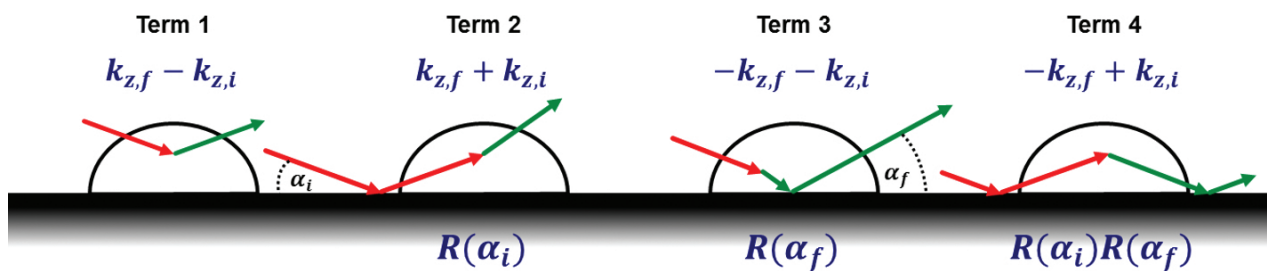


Figure 3. Schematic representation of the four terms involved in the scattering of a supported object on a solid substrate. The scattering event is represented by the color change of the arrows.

The first term is the simple BA and for $\alpha_{i,f} \gg \alpha_c$ Eq. (8) resembles the BA since $R(\alpha_i) = R(\alpha_f) = 0$. In this case—where the BA is valid and reflection/refraction effects can be neglected—the so-called effective layer approximation can be used and the differential cross-section for diffuse scattering can be written as [24, 25]:

$$\frac{d\sigma}{d\Omega}|_{diff} = \frac{C\pi^2}{\lambda^4} (1 - n^2) |T_i|^2 |T_f|^2 P(\vec{q}) \propto P(\vec{q}) \quad (9)$$

where C is the illuminated surface area, λ the wavelength, $T_{i,f}$ the Fresnel transmission functions and $P(\vec{q})$ is the diffuse scattering factor. Within this simplification, the diffuse scattering factor can be expressed in terms of the product of a form factor $F(\vec{q})$ of individual scattering objects and a structure factor $S(\vec{q}_{\parallel})$ that accounts for the spatial arrangement of the scattering objects on the substrate surface and the interference between individual scattering events.⁶ The structure factor is the Fourier transform of the so-called pair correlation

⁵ In the more general case, transmission has to be taken into account and the Fresnel transmission coefficients appear also in the expression of the form factor. See, e.g., [22, 23].

⁶ For this reason, the structure factor, $S(\vec{q}_{\parallel})$, is also often called interference function.

function $g(r)$ that describes the spatial arrangement of scattering entities in real space and several ad hoc pair correlation functions can be used to analyze the GISAXS data.⁷ The diffuse scattered intensity $I(\vec{q})$ for a lateral electron density fluctuation on the surface can be then expressed as

$$I(\vec{q}) \propto \langle |F_{DWBA}(\vec{q})|^2 \rangle S(\vec{q}_{\parallel}) \quad (10)$$

In highly diluted systems $S(\vec{q}_{\parallel})$ tends to 1 since there is no interference between the scattered photons. In these cases, the scattering pattern—being only proportional to $F(\vec{q})$ reflects the shape of the scattering objects. Opposite, in the case of concentrated systems $F(\vec{q})$ and $S(\vec{q}_{\parallel})$ are strongly correlated.

2.3. Coupling of form and structure factors: approximations

Although sometimes useful for the analysis of horizontal line cuts—i.e., the intensity distribution as a function of q_y at constant q_z extracted from the 2D scattering pattern—the expression derived for the diffuse scattering intensity in the previous section (Eq. (10)) is a crude simplification since small angle scattering is comprised of a coherent term, which is the product of the form factor and structure factor, and an incoherent one that appears as a consequence of polydispersity in the size distribution of the scattering objects. The incoherent term weaves the form and structure factors and is very difficult to evaluate analytically, thus several approximations have been developed to consider the correlation between the scattering objects and their spatial positions.

The simplest one is the so called decoupling approximation (DA) that assumes that there is no correlation between the kind of scattering object and its position. This approximation is usually applied when the size polydispersity is small or the surface density of scattering entities is low (**Figure 4(a)**).

Opposite to DA, when the polydispersity is high, a full correlation of the size of the scattering object and its position is assumed in the local monodisperse approximation (LMA). LMA considers that within the coherence length of the X-ray beam neighboring objects present the same size and shape, i.e., the polydisperse scattering objects are clustered in monodisperse domains whose scattering intensities are incoherently summed up (**Figure 4(b)**).

In between these extreme cases, the size-spacing correlation approximation (SSCA) [26] was developed to account for more realistic correlations between the size and separation of the scattering entities. Its formalism is derived from the paracrystal theory and introduces a partial correlation of sizes and positions in a probabilistic way. Shortly, within the SSCA, given a scattering object of distinct size and position and a description of the size polydispersity by a

⁷ Some of the more commonly applied are the Debye hard core interference function, the Gaussian pair correlation function, the gate-pair correlation function, the Lennard-Jones pair correlation function, etc. See [12] and references therein.

statistical function, the probability of finding neighboring objects of particular size and positions with respect to the first scattering object is obtained, considering a particular probability distribution. Thus, both size-dispersion and position disorder are propagated statistically along the arrangement of scattering entities and long-range order is gradually destroyed in a probabilistic way (**Figure 4(c)**).

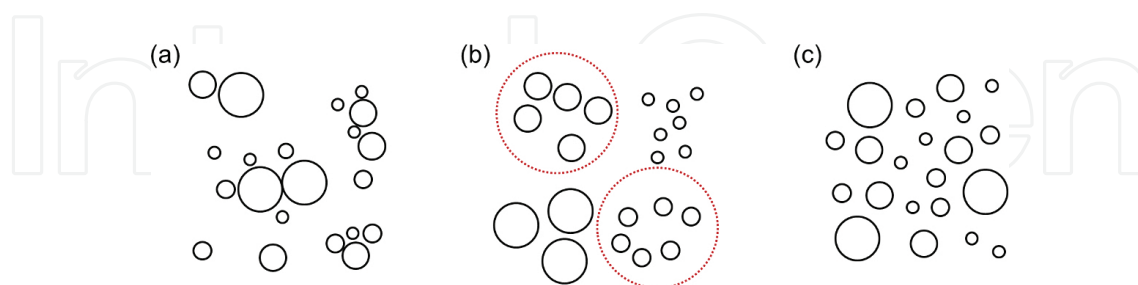


Figure 4. Schematic representation of the size-space correlation of scattering entities within (a) the decoupling approximation (DA), (b) the local monodisperse approximation (LMA), and (c) the size-spacing correlation approximation (SSCA). In (b), the red dotted circles represent the coherent X-ray domains.

3. In-situ GISAXS during deposition processes

During the last decade or so, GISAXS has been established as a very powerful technique to reveal the kinetics of deposition processes for thin film preparation employing different approaches. In particular, GISAXS is strongly contributing to reveal the mechanism of thin film growth and self-assembly both for vacuum and wet deposition processes that are relevant not only from a fundamental point of view but also for technological development. GISAXS presents two decisive advantages over standard microscopic techniques for the investigation of the growth kinetics and self-assembly: first, it provides averaged information over a large sample area—the beam footprint on the sample—thus the information acquired is of statistical significance; second, time resolutions down to several milliseconds are accessible due to the high X-ray intensities offered by third-generation synchrotron sources and the development of fast 2D X-ray detectors, thus fast kinetic processes can be studied.

In this section, exemplary results will be presented illustrating the strong capabilities of in-situ time-resolved GISAXS for the investigation of the stages governing the kinetics of thin film growth and self-assembly, both phenomena of high importance to gain control over the processes so as to tune the thin film properties to the required functionality.

3.1. Vacuum deposition of nanostructured metallic thin films

Vacuum deposition of nanostructured metallic films constitutes a very important technological and research field with applications ranging from coatings for antibacterial activity and catalysis to plasmonics, optoelectronics and sensors. In most cases, the morphology is closely related to the functionality of the film. Therefore, it is extremely important to achieve a deep

understanding of the growth mechanism and morphological development of the nanostructures so as to allow for tailoring the nanostructured metallic thin film to the desired application.

In order to investigate in-situ vacuum deposition processes using GISAXS, deposition chambers have been specifically designed to be installed at synchrotron beamlines [27–29]. In addition, a growing amount of systems have been investigated during the last years—some examples can be found in [30–33]—from which, in the following, only some selected results will be discussed.

In-situ μ GISAXS has been applied to study the sputter deposition process of both Au and Ag on SiO_x with time resolutions of 15 and 100 ms, respectively [34, 35]. The growth kinetics of these two systems has been probed to proceed in a similar way and in-situ μ GISAXS has contributed to elucidate the growth regimes and the associated kinetic thresholds of the systems. The analysis of the temporal evolution of the main scattering features—namely the position and full-width-at-half-maximum (FWHM) of the out-of-plane scattering peak (line cuts of the 2D scattering pattern along q_y at constant q_z) together with the evolution of the scattering profile of the so-called detector cuts and off-detector cuts (line cuts of the 2D scattering pattern along q_z at $q_y = 0$ and at constant $q_y \neq 0$, respectively)—led to identify four different growth stages dominating the morphological development of Au and Ag thin films, from the nucleation phase to the formation of a complete layer (Figure 5).

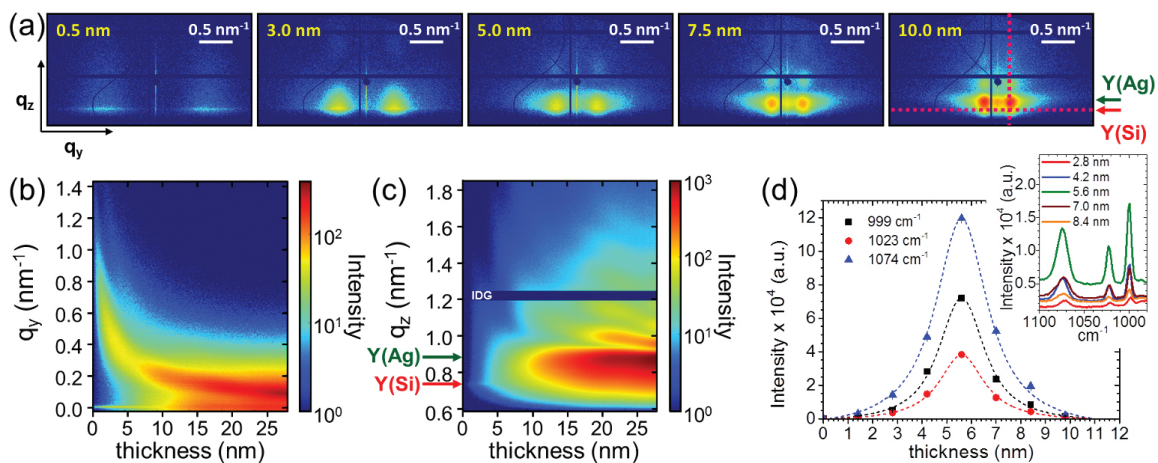


Figure 5. (a) Selected 2D μ GISAXS patterns during sputter deposition of Ag on SiO_x . The deposition process was continuously monitored with a time resolution of 100 ms. The effective film thickness is indicated in each GISAXS pattern. The dotted lines on the right pattern mark the positions where line cuts were performed to evaluate the data. (b) Out-of-plane (along q_y) line cuts versus sputtered thickness at the Si Yoneda peak ($q_{z,c}(\text{Si}; 13 \text{ keV}) = 0.733 \text{ nm}^{-1}$). The evolution of the out-of-plane scattering peak from large q_y toward lower values is related to an increase in the mean distance between Ag nanoclusters as a consequence of the increase in clusters size. When the percolation threshold is reached, the peak gets arrested at a nearly constant value. A quantitative analysis of the mean distance D between nanoclusters can be performed from the peak maximum applying $q_y \approx 2\pi/D$. (c) Off-detector (along q_z) line cuts versus sputtered thickness at $q_y = 0.112 \text{ nm}^{-1}$. As the deposition proceeds, the maximum intensity changes from the Si Yoneda peak to the Ag Yoneda peak and vertical modulations related to the formation of Ag layers appear. (d) Intensity of the characteristic SERS bands of thiophenol shown in the inset for different Ag thickness. The dashed lines are Voigt fittings to the data. IDG: intermodule detector gap. Y(Si): Si Yoneda peak. Y(Ag): Ag Yoneda peak. Adapted with permission from Santoro et al. [35] with the permission of AIP Publishing.

The growth kinetics of Au during sputter deposition, apart from being of industrial and technological relevance, is of significant importance from a basic point of view. To simulate the complete 2D μ GISAXS patterns along the deposition process, a geometrical model based on the 2D hexagonal paracrystalline arrangement of hemispherical clusters was developed [34] allowing for extracting important parameters such as the surface coverage, film porosity or cluster density, thus enabling to predict morphology-dependent properties of the thin film such as the optoelectronic response.

Since the growth of Ag on SiO_x proceeds in a similar manner, the geometrical model proposed by Schwartzkopf et al. [34] has been also successfully applied to the deposition of nanostructured Ag thin films on SiO_x for surface enhanced Raman spectroscopy (SERS) (**Figure 5(d)**) [35]. A key point in SERS, whose underlying main mechanism is the enormous enhancement of the local electromagnetic field in the vicinity of nanostructured noble metal surfaces due to localized surface plasmons, is the gap between nanostructures. At the nanostructure gaps—the so-called “hot-spots”—the electromagnetic enhancement is maximum. In this case, in-situ μ GISAXS during sputter deposition of Ag allowed not only identifying the main growth regimes and thresholds but also to correlate the developed morphology to the SERS activity. By modeling the full 2D μ GISAXS patterns within the DWBA and the SSCA, a maximum SERS enhancement was found for a mean gap of 1 nm between Ag nanoclusters, corresponding to an effective film thickness of 5.6 nm.

On the other hand, the deposition kinetics of Au on a quasi-regular hexagonal array of self-assembled cadmium selenide (CdSe) quantum dots has also been investigated by in-situ μ GISAXS [36]. Opposite to the growth of Au and Ag on SiO_x , in the early deposition stage the out-of-plane peak did not change in position but remained fairly constant. The deposition of Au only led to an increase in electronic contrast, thus, of the diffuse scattering intensity produced by the underlying array of CdSe quantum dots. This implies that the quantum dots act as nucleation sites for Au growth. Subsequently, lateral growth and coalescence of Au/CdSe-dot clusters were observed forming a compact Au/CdSe-dot layer. Finally, Au growth proceeded in the surface normal direction developing a capping layer on the CdSe quantum dots array.

In-situ GISAXS has also contributed to shed light on an intriguing issue during the growth of metallic thin films, namely the influence of the chemical affinity between the metal and the substrate on the deposition kinetics and thin film morphology. This is highly important in the case of, e.g., the deposition of metallic electrodes on organic solar cells or light emitting diodes where, in some cases, the electrodes represent the limiting factor in device performance. The great capabilities of in-situ GISAXS studies for this purpose has been demonstrated during the sputter deposition of Al and Ag on tris(8-hydroxyquinolinato)aluminum (Alq3), a key material in organic light emitting diodes. Alq3 presents a strong chemical interaction with Al whereas it interacts weakly with Ag, which translates into different growth mechanisms. In the case of Al deposition, three different stages of growth were identified and modeling of the 2D patterns revealed the formation of Al nanopillars after diffusion of Al in Alq3 and subsequent metal complex agglomeration [37]. On the other hand, without diffusing into the Alq3 thin film, Ag presents a morphological transition from truncated sphere clusters to cylindrical nanostruc-

tures upon surpassing the Ag percolation threshold at an effective film thickness of 5.0 nm (**Figure 6**), which was attributed to the different Ag-Ag and Ag-Alq3 interactions [38].

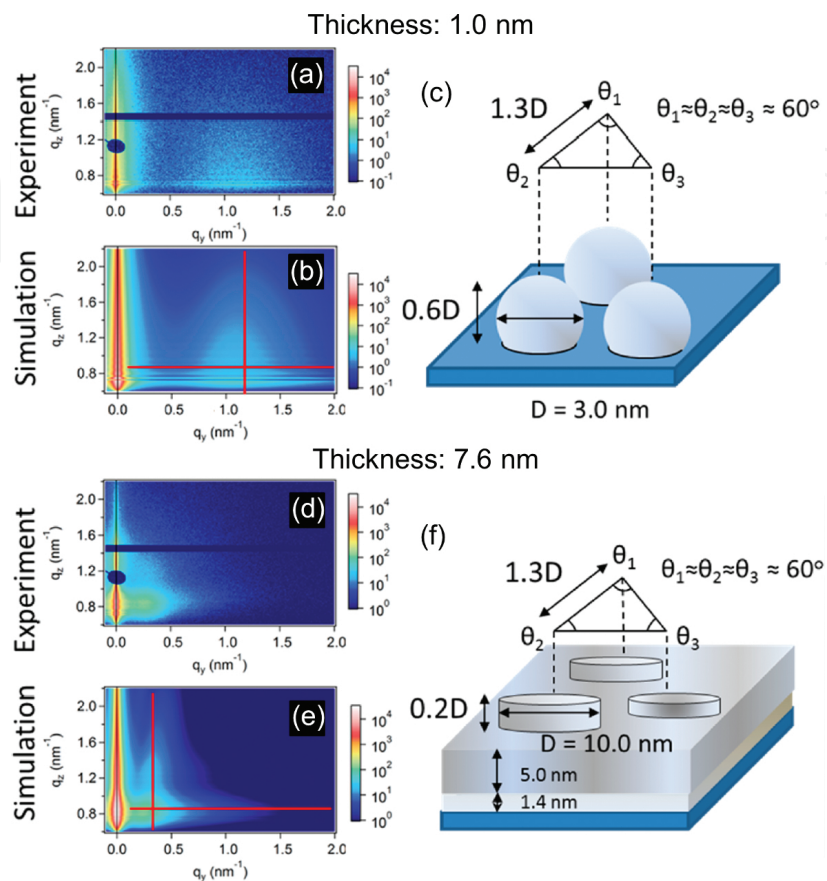


Figure 6. Morphological transition in cluster shape upon surpassing the percolation threshold (effective film thickness of 5.0 nm) during sputter deposition of Ag on a 36.0 nm thick Alq3 film. (a–c) Experimental 2D μ GISAXS pattern, simulated 2D μ GISAXS pattern and geometrical model used to simulate the data, respectively, at an effective Ag film thickness of 1.0 nm. (d–f) Experimental 2D μ GISAXS pattern, simulated 2D μ GISAXS pattern and geometrical model used to simulate the data, respectively, at an effective Ag film thickness of 7.6 nm. In both cases, the DWBA and the LMA were employed to simulate the scattering patterns. Adapted and reprinted with permission from Yu et al. [38]. Copyright 2015 American Chemical Society.

The differences in metal interaction and nanocluster diffusion coefficient on different materials can be exploited to tailor the thin film morphology. In this sense, an interesting approach consists in employing polymer thin films as templates in the nanoscale, given the known ability of block copolymers to spontaneously form nanostructures due to phase segregation. In general, when employing vacuum deposition of metals on organic thin films, in a first deposition stage, the metal diffuses into the film which influences the subsequent growth kinetics and, in the case of block copolymers, a selective wetting of the metal on one of the domains is commonly observed, which is ascribed not only to the different metal-polymer interaction but also to the differences in metal diffusion in each of the blocks. From in-situ μ GISAXS measurements, the surface diffusion coefficient of Au on polystyrene (PS) has been extracted and a correlation of the developed Au morphology with the optical properties of the

film could be achieved by combining μ GISAXS with real-time UV-Vis spectroscopic measurements during the growth [39].

On the other hand, Metwalli et al. [40] have taken advantage of the selective wetting of Co on spontaneously nanostructured polystyrene-block-poly(ethylene oxide) (PS-*b*-PEO) to prepare ordered Co nanoclusters along highly oriented PS domains. The morphology of the polymer thin film consisted of alternating highly oriented crystalline PEO and PS domains with a periodicity of around 30 nm and the in-situ GISAXS experiments demonstrated that selective wetting occurred below the Co thin film percolation threshold. They also elucidated the growth kinetics of Co on the block co-polymer nanostructured template.

A thorough study on the nanostructure development of transition metals on a PS-*b*-PEO template has also been recently reported [41]. It has been clearly revealed that the growth of Au, as a fairly inert element, was not influenced by the template, whereas Ag demonstrated slightly improved wetting on the PS domain, forming clusters. In the case of reactive metals, e.g., Fe, Ni, and Pt, well-defined and uniform nanocluster patterns were grown selectively on the PS domains. Additionally, by performing in-situ GISAXS experiments, it has been found that the substrate temperature plays an important role in shaping the metal clusters, showing that above the glass transition temperature, T_g , of PS, Ag clusters become more irregular. In addition, for Fe, flat nanodots with a low surface-to-volume ratio morphology were grown at substrate temperatures above T_g whereas a higher surface-to-volume ratio morphology is obtained for a substrate at room temperature during deposition. This is ascribed to the changes in diffusion coefficient with temperature, so that above T_g a higher diffusion coefficient of metal atoms and clusters during the deposition led to a lower surface-to-volume ratio cluster morphology.

The complicated growth kinetics of hierarchical anisotropic gold nanostructures on polystyrene-block-poly(methyl methacrylate) (PS-*b*-PMMA) thin films has been also studied with in-situ GISAXS [42]. An anisotropic shape of the deposited metal clusters was achieved by employing a glancing angle deposition (GLAD) geometry. In GLAD, the deposition plume is positioned at an oblique angle regarding the sample surface, which produced nonsymmetric Au clusters and its anisotropic shape manifested as nonsymmetric 2D scattering patterns with respect to the scattering plane ($q_y = 0$). In addition, a hierarchical ordering of the anisotropic Au was achieved benefiting from the selective wetting of Au on the PS domains. The anisotropy of this hierarchical nanostructure was also reflected in the anisotropic optical response of the system.

3.2. Vacuum deposition of organic thin films

Organic thin films are especially important since they are increasingly used in devices. In particular, organic semiconductors are employed in organic light emitting diodes (OLEDs), organic field-effect transistors (OFETs), and organic solar cells (OSCs). However, the basic processes of molecular thin film growth are still far from being understood and connecting molecular and nanoscopic/microscopic processes such as molecular diffusion and island size evolution, remains a major challenge. To this purpose in-situ GISAXS, being a non-invasive technique, is increasingly contributing.

As in the case of vacuum deposition of metals, several organic deposition chambers have been designed and built so as to perform in-situ X-ray scattering and/or diffraction measurements at synchrotron beamlines [43, 44].

To study these particular systems, in-situ grazing incidence X-ray diffraction (GIXD) and in-situ X-ray reflectivity (XRR) are most commonly applied [45–48], though the information provided by in-situ GISAXS is also very valuable since the dimensions probed are different. Whereas GIXD provides access to the crystal structure and molecular arrangement, GISAXS gives complementary information on the island shape and island-island distances as well as on the island electron density. Therefore, the combination of both techniques provides the necessary information to make a link between the molecular and micrometer size crystallite regimes.

These systems are usually investigated in the so called anti-Bragg geometry, i.e., at incident angles so that the specular peak corresponds to the anti-Bragg point of a given $(h\ k\ l)$ permitted Bragg reflection of the molecular crystalline structure. The anti-Bragg points correspond to $|\vec{q}_{\text{anti-Bragg}}| = \frac{1}{2} |\vec{q}_{\text{Bragg}}|$ and are especially surface sensitive⁸ [17]. From a practical point of view, for a selected $(h\ k\ l)$ Bragg reflection, α_i is chosen so that at $\alpha_i = \alpha_f$ and $\psi = 0$ – i.e., the specular peak position – the following relationship is satisfied

$$q_z = \frac{2\pi}{\lambda} (\sin(\alpha_i) + \sin(\alpha_f)) = \frac{4\pi}{\lambda} \sin(\alpha_i) = \frac{1}{2} |\vec{q}_{\text{Bragg}}| \quad (11)$$

Note that in Eq. (11) only q_z is involved since for specular reflection $q_x = q_y = 0$ (Eq. (1)).

At this particular geometry, the specular intensity presents an oscillatory behavior during the growth—the so-called growth oscillations—which arises from destructive interference between neighboring odd and even monolayers (MLs) —lattice planes—so that the scattering from the first, third, fifth ML is cancelled by the growth of the second, fourth, sixth ML, etc. [49]. In the common case of (initial) layer-by-layer growth in organic heteroepitaxy, the periodicity of the oscillations consists in 2 MLs although interference between reflections at the growing surface, the substrate and the interfaces between different film layers can lead to more complex oscillatory behavior.⁹ Through correct modeling of the growth oscillations, more complicated epitaxy growth models can be derived making assumptions about the intralayer and interlayer diffusion [50]. Therefore, additional information for the refinement of these models is very useful and can be obtained by performing GISAXS at the anti-Bragg geometry, which allows concurrently following the changes in the specular intensity—the growth oscillations—and the diffuse scattering [51–54].

⁸ An introduction to surface X-ray diffraction, including the evanescent wave method that corresponds to GIXD, can be found in [17].

⁹ For instance, considering an out-of-phase reflection on the substrate, the oscillations maxima appear at even instead of at odd numbers since an additional reflection occurs or, e.g., the oscillations period can change to 1 ML in the case of homoepitaxy. See [49].

The abovementioned geometry has been applied to investigate, e.g., the growth of multilayers of fullerene C_{60} molecules on mica in real time [55]. From the growth oscillations, a layer-by-layer growth was deduced whereas from the in-situ μ GISAXS data the mean island distance was extracted and converted into surface island density assuming a hexagonal island arrangement. Interestingly, the GISAXS out-of-plane peaks present intensity oscillations with a period of 1 ML, in contrast to the 2 ML period of the specular intensity at the anti-Bragg point (**Figure 7**). This is due to the fact that diffuse scattering occurs only for uncomplete layers since this is the situation where a lateral variation in electron density—or, in other words, in refractive index—is present, whereas the growth oscillations are due to interference from the reflections at layer interfaces—plus at the substrate and at the growing layer—i.e., diffuse scattering is probing lateral contrast whereas the specular peak probes the structures in the surface normal direction. Through kinetic Monte Carlo simulations and a comparison to the experiments, values of the energy barriers were obtained—namely, the diffusion barrier and lateral binding energy for intralayer events and an Ehrlich-Schwoebel barrier for interlayer diffusion—and, more importantly, this set of parameters was demonstrated to be sufficient to describe the growth of a C_{60} layer on underlying C_{60} layers, of crucial importance so as to predict the growth dependence on the deposition rate and substrate temperature.

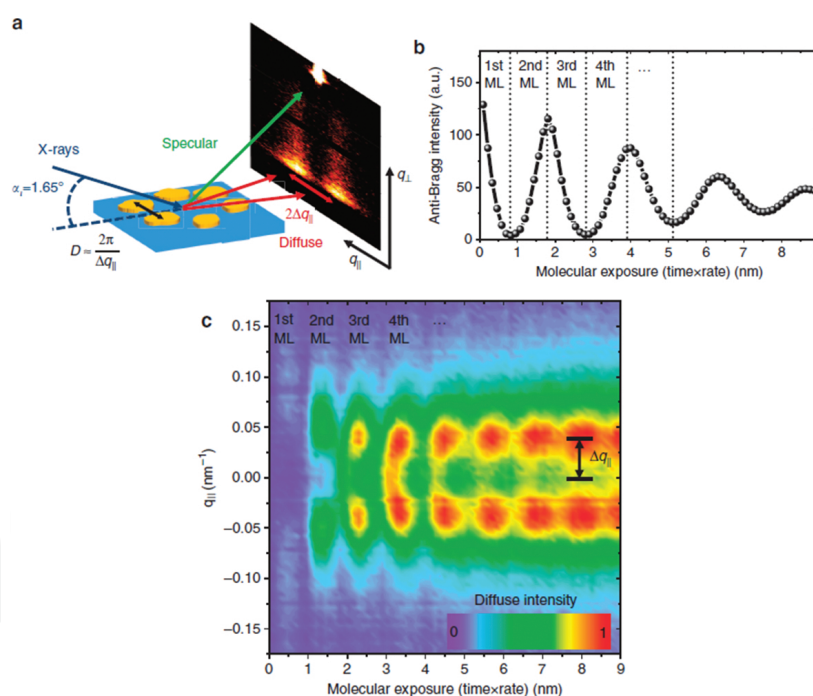


Figure 7. (a) Scattering geometry employed showing the simultaneous acquisition of specular and diffuse scattering. The incident angle is chosen so that the specular peak corresponds to the anti-Bragg position of the C_{60} (1 1 1) reflection. (b) Intensity at the anti-Bragg point $q_z = 0.38 \text{ \AA}^{-1}$ as a function of the molecular exposure during the film growth. A damping of the growth oscillations from the third monolayer on is due to surface roughening since an imperfect layer-by-layer growth for high number of MLs occurs, providing a measurement of the roughening onset. (c) Oscillations of the out-of-plane GISAXS intensity as a function of the molecular exposure. From the out-of-plane peak position, the mean island distance can be extracted by $q_y \approx 2\pi/D$. © 2014 S. Bommel, N. Kleppmann, C. Weber, H. Spranger, P. Schäfer, J. Novak, S.V. Roth, F. Schreiber, S.H.L. Klapp and S. Kowarik. Adapted with permission from Bommel et al. [55]; originally published under Creative Commons Attribution 4.0 License. Available from: 10.1038/ncomms6388.

The simultaneous acquisition of the specular intensity and GISAXS signal has also been applied to in-situ investigate the molecular diffusion and island evolution during the growth of diindenoperylene (DIP, $C_{32}H_{16}$) on SiO_x [56]. Opposite to the C_{60} molecule, DIP presents shape anisotropy imposing additional degrees of freedom—tilting and bending—which increases the complexity of the growth process. In this case, above a surface coverage of 3 MLs the GISAXS out-of-plane peak oscillations vanished and the peak position remained constant, meaning a constant island center-to-center distance. This is a clear signature of a transition between a layer-by-layer to a three dimensional (3D) growth, i.e., formation of molecular islands with a fixed surface island density. Additionally, effective activation energies for island nucleation of DIP on SiO_x and of DIP on DIP could be extracted from the mean island diameter—derived from the diffuse scattering peak position—at 0.5 ML and 1.5 ML surface coverage, respectively, by varying the deposition substrate temperature.

Another organic semiconductor with rod-like morphology whose growth has been in-situ investigated performing GISAXS using the anti-Bragg geometry is *N,N'*-dioctyl-3,4,9,10-perylene tetracarboxylic diimide (PTCDI- C_8 , $C_{40}H_{42}N_2O_4$) [57]. It has been shown that PTCDI- C_8 , as is the case for DIP, underwent a transition from a layer-by-layer growth to a 3D growth but in a smoother fashion. This manifested both as a slow increase in the mean roughness of the completed MLs—derived from the growth oscillations—as well as in a smooth leveling off of the island density—derived from the out-of-plane GISAXS peak position by assuming a hexagonal arrangement of islands. Moreover, the island density extracted from the diffuse scattering at different substrate temperatures, allowed demonstrating higher molecular mobility of PTCDI- C_8 on PTCDI- C_8 than that of PTCDI- C_8 on SiO_x , which is responsible for the decreased island density observed in upper MLs.

3.3. Wet deposition of polymer and colloidal thin films

Wet deposition encompasses a collection of different methods for the fabrication of thin solid films from a liquid solution and/or suspension as precursor. All of them exploit self-assembly concepts to prepare thin films such as colloidal crystals, thin polymer films and nanocomposites with applications ranging from photonic crystals to polymer solar cells and superhydrophobic or superhydrophilic coatings. During wet deposition, the interaction between the suspended particles—or the dissolved compounds—together with the liquid flow—responsible of internal mass transport—govern the drying kinetics and self-assembly. Hence, tuning these parameters makes it possible to control the self-assembly, thus adjusting the morphology of the dried thin film (ideally) on demand.

Grazing incidence X-ray scattering (GIXS) techniques has been applied to study wet deposition processes such as solution casting [58, 59], spin-coating [60], dip-coating [61, 62], and blade coating [63]. Nevertheless, although these deposition methods are very useful for device fabrication at research scale, they are not easily scaled-up and/or they are restricted to specific substrate geometries. In this sense, it is important to explore other wet deposition methods of potential industrial relevance.

In recent years, spray coating is gaining interest due to its easy scale-up and integration into production lines as well as to its lack of substrate geometry/size constraints. Moreover, it has

already been successfully applied to fabricate operating devices such as polymer solar cells [64–66]. Nevertheless, although there are evident similarities to, e.g., solution casting, the drying kinetics present some particularities still not well understood. To this respect, GISAXS has been used to study the self-assembly of colloidal particles during spray coating [65, 67, 68]. In particular, Herzog et al. [67] were able to identify three different stages during the spray deposition of polystyrene (PS) nanoparticles and subsequent drying corresponding to the formation of a structureless thin liquid film, which subsequently breaks up into small droplets allowing for possible transient nanoparticle ordering and a final freezing of a self-assembled colloidal nanostructure once the solvent is fully evaporated, respectively. These three stages were revealed in the in-situ μ GISAXS patterns as first, a decrease in the overall scattered intensity due to the homogeneous liquid film right after a 100 ms spray shot; second, an increase and broadening of the Yoneda peak ascribed to the homogeneity loss of the liquid film that breaks into small droplets as the solvent evaporation proceeds and last, the emergence of well-defined out-of-plane symmetric peaks regarding the scattering plane (**Figure 8**). In addition, controlling the evaporation rate by adjusting the substrate temperature the assembly process of the nanocolloids can be managed to achieve different film morphologies, what has been investigated in-situ by μ GISAXS as well [68].

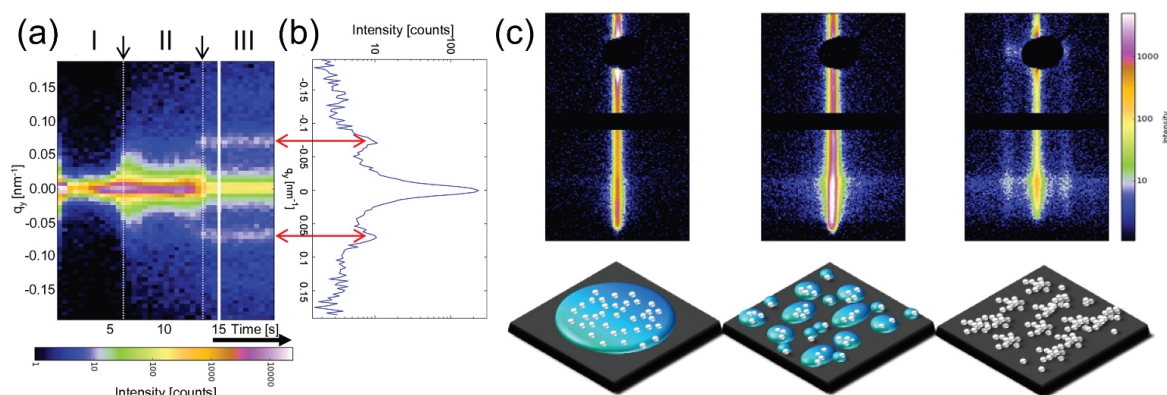


Figure 8. (a) Out-of-plane cuts (along q_y) at the Si Yoneda peak ($q_{z,s}(\text{Si}; 13 \text{ keV}) = 0.733 \text{ nm}^{-1}$) as a function of time during spray deposition of PS nanoparticles with a nominal diameter of 100 nm. The vertical dotted lines indicate the transitions between drying stages. (b) Individual out-of-plane cut of the dried sample at 15 s after spray deposition displaying side maxima corresponding to the most prominent lateral length scale of $\approx 90 \text{ nm}$. (c) Representative 2D GISAXS patterns of each of the three identified drying stages. Below each pattern a sketch of the corresponding drying stage in real-space is depicted. Reprinted (adapted) with permission from Herzog et al. [67]. Copyright 2013 American Chemical Society.

Apart from spray coating, another interesting approach for large scale low-cost production of organic photovoltaic (OPV) devices is inkjet printing, a method that has drawn considerable attention from an industrial point of view as the field of organic flexible electronics is maturing. As in the case of spray coating, GIXS has been applied to in-situ investigate the structure development during inkjet printing of, e.g., conductive polymer thin films widely used as electrodes in OPV devices [69] as well as of the active layer in bulk-heterojunction (BHJ) polymer solar cells [70]. The film morphology in OPV devices has a direct relationship with its performance and the combination of in-situ wide- and small angle scattering (GIWAXS/

GISAXS) allowed developing qualitative models of the structural evolution of the semicrystalline polymer thin films morphology.

Finally, although it does not present the current large-scale production promises of spray coating and inkjet printing, an interesting approach for wet deposition consist in employing microfluidics, which may be critical for lab-on-chip applications. Here, the peculiarity lies in the nondrying nature of the deposition, i.e., the self-assembly process on the substrate does not take place during solvent evaporation but at the liquid-solid interface during liquid flow. In order to in-situ follow deposition processes using microfluidics by GISAXS—among others; see Section 4—special flow cells have been designed [71]. In this kind of experiments, it is extremely important to adjust the X-ray beam footprint on the substrate to the size of the fluidic channel so as to prevent an overillumination of the sample not in contact with the fluid, thus minimizing undesired signal that could obscure the accessible information. Therefore, the use of μ GISAXS becomes essential [72]. This specific setup has been used to investigate the attachment of Au nanoparticles to a polymer thin film (**Figure 9**) and different stages could be identified, namely the dried polymer film before the liquid inlet was opened (denoted as 1 in **Figure 9**), a wetted film by the liquid vapor once the liquid inlet was opened (denoted as 2 in **Figure 9**) and the attachment of Au nanoparticles once the liquid flow reached the probed thin film position (denoted as 3 in **Figure 9**). Moreover, the increase in intensity of the out-of-plane peak as the experiment proceeded indicated a cumulative deposition of the Au nanoparticles from which it is possible to analyze the deposition kinetics.

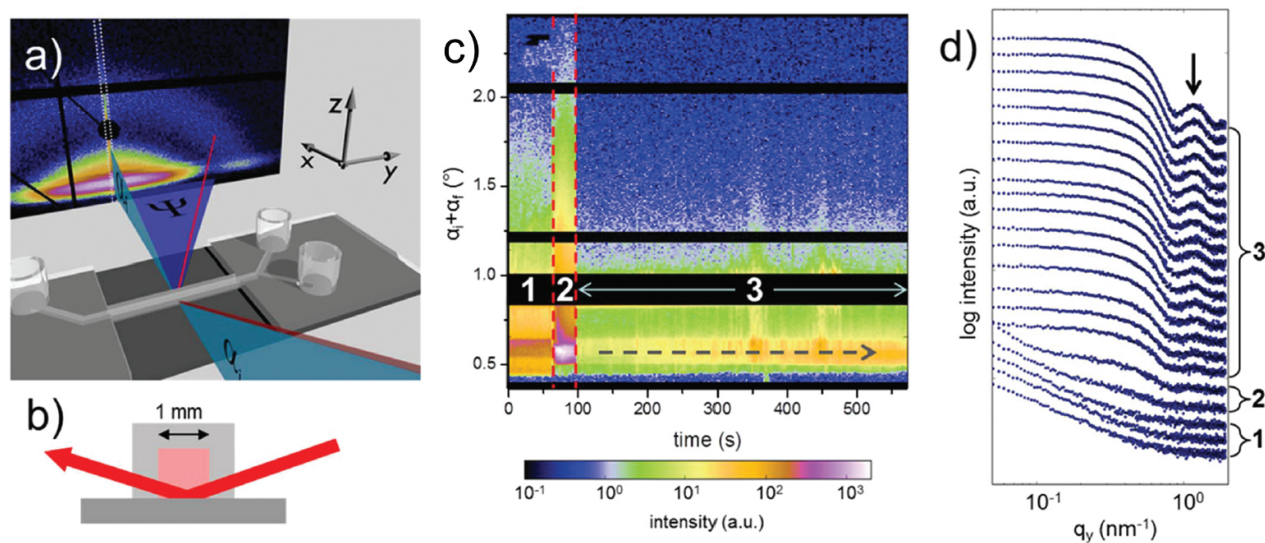


Figure 9. (a) Sketch of the μ GISAXS setup with microfluidic cell. (b) Illustration of the X-ray beam transmitting the channel walls and the footprint on the sample surface. For clarity the incident angle and X-ray beam size are not in scale. (c) Detector cuts (along q_z at $q_y = 0$) as a function of time while 10 nm diameter Au nanoparticles attach to a poly(ethyleneimine) (PEI) thin film on a SiO_x substrate. Black regions correspond to the specular beamstop and the intermodule detector gaps. (d) Out-of-plane cuts (along q_y) at the Si Yoneda peak ($q_{z,c}(\text{Si}; 13 \text{ keV}) = 0.733 \text{ nm}^{-1}$) as sum of 10 consecutive measurements. The curves are vertically shifted for clarity. The numbers denote the deposition stages. Reprinted from Santoro et al. [72], with the permission of AIP Publishing.

4. In-situ GISAXS during thin film processing

In addition to the aforementioned deposition processes, a different kind of studies in which in-situ GIXS is increasingly contributing consist in thin film processing. GIXS has been performed during thin film nanostructuring in order to gain insight into the morphology transformation processes, e.g., metal nanocluster formation through high temperature annealing induced dewetting [73, 74], dewetting of organic multilayer films [75], or refinement of block co-polymer thin film morphology during solvent vapor annealing [76]. Furthermore, working devices have also been investigated by in-situ GIXS so as to identify the structural changes that the active thin film undergo during operation with the aim of improving the device design and final performance, e.g., catalysis on nanoparticles [77], roughening of surfaces during electrodeposition [78], electrochemistry in ionomer matrices of interest in fuel-cell devices [79], or BHJ polymer solar cells [80, 81]. As in the previous section, the development of specific environmental cells to be installed at synchrotron beamlines commonly constitutes a prerequisite to conduct this kind of experiments. In the following, we will shortly describe some recent exemplary results of in-operando and in-situ GISAXS during thin film processing.

As mentioned in the previous paragraph, a well-known way of producing – or modifying the morphology of – metal nanoclusters on a surface consists in the thermal induced dewetting of metallic thin films. This process has been in-situ investigated by GISAXS for the case of Au on Si (1 1 1) up to the bulk eutectic point T_e of the Au/Si system [82]. After the deposition of Au thin nanostructured films by thermal evaporation, a linear increase of the mean distance between Au nanoclusters was observed – associated to an increase in cluster size – together with an increase in the mean cluster height as the temperature approached T_e , which jointly translated to an increase in the contact angle of the nanoclusters. More interestingly, from the Au nanoclusters contact angle at T_e , the liquid-solid interface tension of nanometer-sized Au clusters was calculated and it was found to be larger than that of macroscopic Au droplets on Si (1 1 1). Additionally, the work of adhesion of an Au nanodroplet at the system eutectic point was derived.

In the case of semiconductor materials, ion beam bombardment is a very useful process to induce surface nanostructuring. During the erosion of a surface by accelerated ions, the produced instabilities can lead to the formation of self-assembled patterns of nanostructures and different surface topographies can be obtained as a function of the ion mass, ion energy and bombardment geometry. In-situ GISAXS with partially coherent X-ray beams (Co-GISAXS) has been employed to study the nanodot formation on a gallium antimonide (GaSb) (0 0 1) surface by normal incidence bombardment of 500 eV Ar ions [83]. The use of partially coherent beams allows not only accessing the kinetic phenomena but also the dynamics. Under a coherent illumination, the scattered intensity consists of a speckle pattern (**Figure 10**) and the speckle distribution and speckle intensity fluctuations reflect the underlying dynamics of the surface morphology [84]. From a kinetic point of view – GISAXS analysis – the mean size and distance of the nanodots as a function of time was extracted and the kinetic regimes and onsets derived. More interestingly, though the characteristic GISAXS signal remained stable after saturation of the nanostructuring process, the dynamics showed that ageing – slow down

of the dynamics—was occurring, mainly ascribed to hindered mass redistribution phenomena. The dynamics was extracted from the speckle analysis through the so-called two-time correlation function that accounts for the fast variation of intensity redistribution within the scattering peak with respect to the averaged intensity distribution over time. Finally, a dynamical transition to a regime dominated by the build-up of stress at the surface was identified.

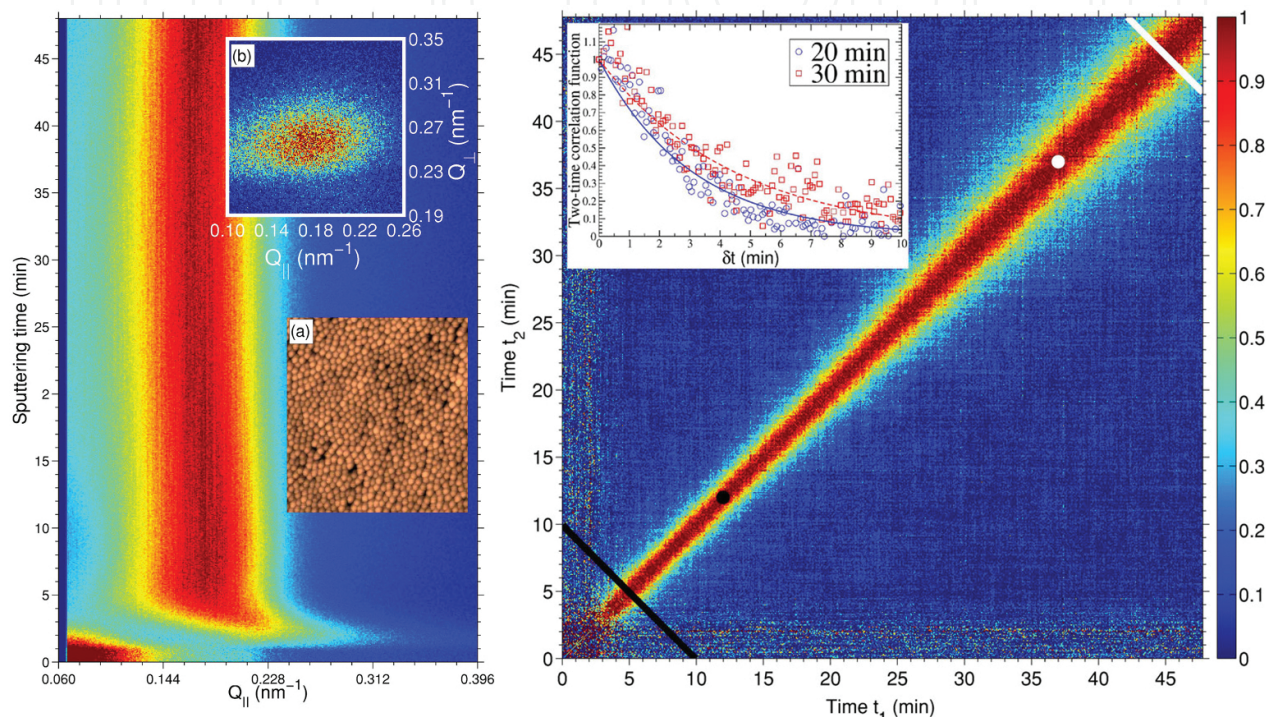


Figure 10. Left: Evolution of the GISAXS out-of-plane peak as a function of ion bombardment time. The onset of surface nanostructuring is evidenced by the emergence of the side peak 1 min after erosion started. After around 5 min the out-of-plane peak remained at constant position revealing the saturation of the nanostructuring process. The upper inset show the speckle distribution within the out-of-plane peak at $t = 47$ min whereas the lower inset shows the real-space morphology as revealed by atomic force microscopy. Right: Normalized two-time correlation function calculated around the out-of-plane GISAXS peak. The black and white lines mark the start and end of aging, respectively, whereas the black and white dots correspond to the average times where a change in the correlation time occurred (change in dynamical regimes). The inset shows cuts of the two-time correlation function as function of $\delta t = t_2 - t_1$ (hollow blue dots and hollow red squares). A good fitting was achieved using exponential decay functions. © 2013 O. Bikondoa, D. Carbone, V. Chamard and T.H. Metzger. Adapted from Bikondoa et al. [83]; originally published under Creative Commons Attribution 3.0 Unported License. Available from: 10.1038/srep01850.

On the other hand, nanostructuring of polymer thin films is an intense field of research and different strategies are being employed, e.g., nanoimprint lithography, porous anodic aluminum oxide (AAO) templating or, as mentioned in Section 3.1, the design of block co-polymer morphologies. An interesting approach consists in the formation of nanostructured surfaces by the so-called laser-induced periodic surface structure (LIPSS) formation, a technique that has been used for years to nanostructure metals and semiconductors but has only recently been applied to polymers [85, 86]. In LIPSS, a pulsed laser of a definite polarization is shined

on the material at fluences (optical energy per surface area) well below the ablation threshold and the material surface gets nanostructured by interference of the incoming and scattered electromagnetic wave through a feeding mechanism not yet well understood. In the common case of linearly polarized incident light the process induces ripple formation on the surface with a periodicity resembling the wavelength of the laser employed. By performing in-situ GISAXS measurements while irradiating a poly(trimethylene terephthalate) (PTT) thin film the onset of ripple formation at different laser repetition rates and fluences has been revealed [87]. Moreover, the results support a feeding mechanism based on a local heating of the polymer thin film so that LIPSS formation becomes more efficient the shorter is the laser pulse separation, whereas for long enough laser pulse separation heat dissipation takes place between pulses hindering the ripple formation.

A different way in which polymer thin films are processed does not consist in the promotion of structuring to tailor the material properties but in the processes that polymeric materials undergo during operation. For instance, in several applications the polymeric material is in contact with fluids, e.g., in the case of polymeric materials used in human implants. Here, the combination of μ GISAXS and microfluidics offers unique capabilities for investigating the morphological changes of polymer thin films in contact with a fluid flow.

A model system comprising of a thin film of sodium alginate with embedded dispersed PS nanoparticles have been investigated by in-situ μ GISAXS during water flow in a microfluidic device [88]. This system served as a model to investigate the detachment of thin films and nanoparticle aggregates therein by a fluid flow, both with and without additional sodium alginate cross-linking. More interestingly, the combination of in-situ μ GISAXS and a microfluidic cell have resulted in the accurate description of the swelling behavior of the thermo-responsive poly(*N*-isopropylacrylamide) (PNIPAM) polymer, a well-known hydrogel when cross-linked [89]. An important feature observed in the GISAXS pattern of soft thin films deposited on rough surfaces is the correlated roughness of the film, i.e., the soft matter thin film present a roughness that replicates that of the substrate. Thus, the film shows X-ray waveguiding effects producing scattering with partial coherence and resonant diffuse scattering is observed [13]. In this case, the diffuse scattering with partial phase coherence coming from the different interfaces concentrates into narrow sheets parallel to the q_x direction and appear in the 2D GISAXS pattern as intensity modulations in the scattering plane (along q_z at $q_y = 0$). These modulations enable a direct determination of the distance between the correlated surfaces by $q_z = 2\pi/d_{\text{corr}}$ (**Figure 11(a) and (b)**). It is important to calculate d_{corr} for large q_z values so that the Yoneda peak intensity does not introduce an additional signal that could distort an accurate determination of d_{corr} . From the in-situ μ GISAXS measurements, neither the thickness nor the topography of the PNIPAM thin film was observed to change during exposure to highly undersaturated water vapor. However, as early as the film is brought in contact with liquid water it starts swelling mostly in a 1D manner, i.e., mainly an increase of film thickness occurs, being the restructuration of the surface topography (surface flattening) slightly retarded but obviously correlated to the swelling process (**Figure 11(c)**).

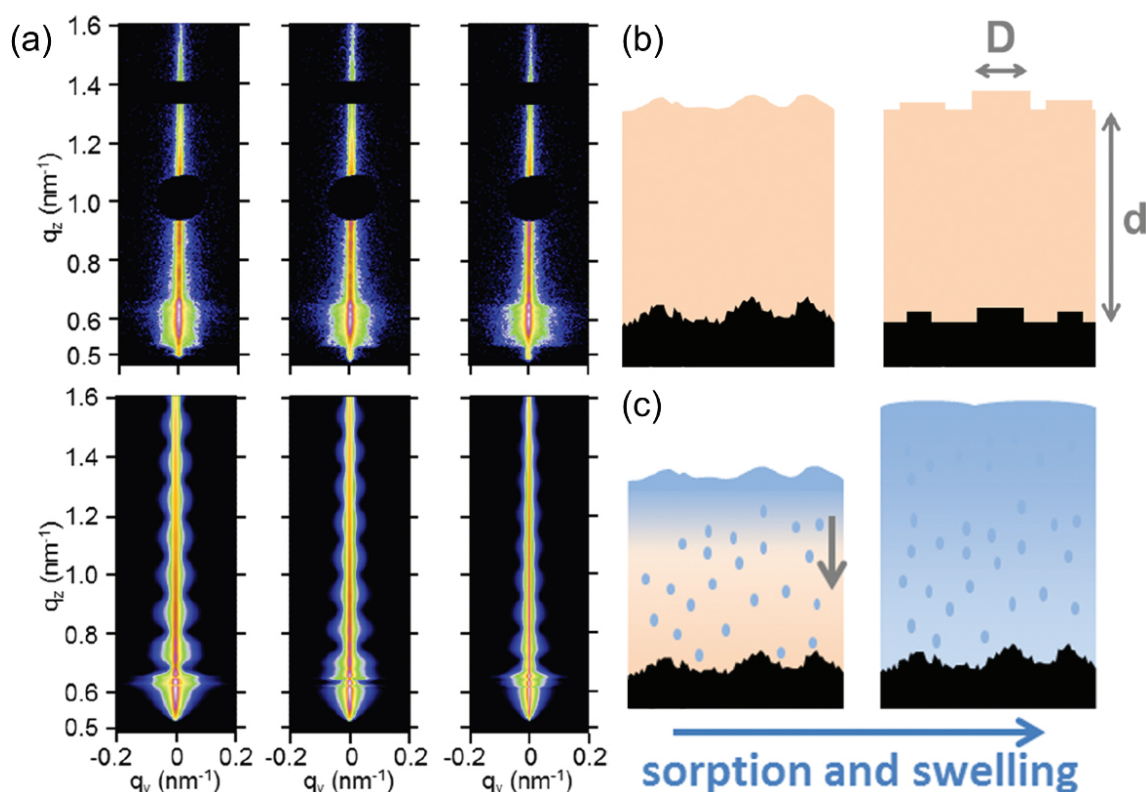


Figure 11. (a) Experimental (upper row) and simulated (lower row) 2D μ GISAXS patterns during swelling of a PNIPAM thin film under water flow in a microfluidic cell. The scattering patterns correspond to exposure to water vapor (left), after 30 s of water flow (middle) and after 48 s of water flow (right). The GISAXS patterns were continuously acquired before and during water flow with a time resolution of 1 s. The DWBA and the LMA were employed to simulate the scattering patterns. (b) Schematic drawings of the glass-supported, as-spun PNIPAM film, possessing partially correlated interfaces (left) and the corresponding morphological model used in the simulations (right). The parameters that were varied to simulate the water uptake process are the thickness of the PNIPAM layer, d , and the diameter of the PNIPAM discs, D . (c) Illustration of the surface restructuring in the course of the swelling of the thin, glass-supported PNIPAM film. Left: sorption of liquid water, filling the accessible free PNIPAM volumes and inducing the devitrification of its near-surface layer. Right: mainly 1D swelling occurs as the gel-glass phase boundary propagates into the depth of the film; the surface flattens as the mobility of the macromolecules is sufficient. Reprinted (adapted) with permission from Philipp et al. [89]. Copyright 2015 American Chemical Society.

Other polymeric thin films that have been investigated by in-situ GISAXS during operation are the active layers of BHJ polymer solar cells (**Figure 12**). In general, although polymer solar cells hold the promise of future low-cost flexible solar cells, a major problem of these OPV devices is the performance loss during operation. In this sense, in-operando μ GISAXS studies have revealed that the active layer suffers from morphological changes during operation [90]. These morphological changes are directly related to the decrease in short-circuit current density (SCCD) that was derived from the simultaneous measurement of current-voltage curves while the device was illuminated by a solar simulator. In order to demonstrate this unequivocal relationship between performance loss and morphological transformation, Monte Carlo (MC) simulations of the SCCD were performed using the structural parameters extracted from modeling of the μ GISAXS patterns. The agreement between the MC simulations and the measured SCCD was excellent (**Figure 12(c)**) concluding that an increase in P3HT

domain size and separation during illumination is responsible for the decrease of effective light harvesting area, thus decreasing the exciton splitting events, whereas the PCBM domain size and distance remained fairly constant. Moreover, a temperature effect was ruled out since the solar cell did not exceed 45°C during the experiments due to Peltier cooling.

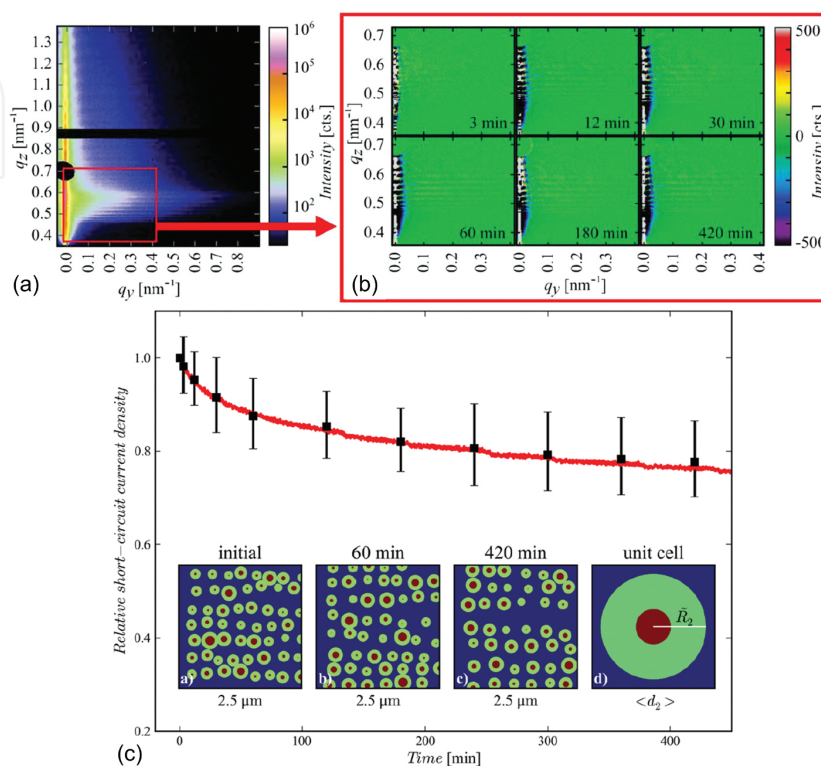


Figure 12. (a) 2D μ GISAXS pattern of the polymer solar cell before illumination. (b) Difference scattering patterns, i.e., 2D μ GISAXS measurements obtained at different operation times after subtraction of the initial scattering pattern within the marked window (red box) in (a). Negative values mean a loss of signal with respect to the initial measurement. (c) Simulated (black dots) and measured short-circuit current density (red line). The simulated short-circuit current density was derived from the morphological parameters extracted by μ GISAXS. The insets show the inner film morphology at different times as generated by the Monte Carlo simulations. The inset on the right presents the domain morphology model used in the simulations and extracted from the μ GISAXS experiments: red correspond to the core of P3HT domains, green to the effective light harvesting area and blue to the non-active effective area of the solar cell. Reproduced with permission from Schaffer et al. [90]. Copyright 2013, John Wiley and Sons.

5. Conclusions

In this chapter, we have reviewed the current trends in the application of time-resolved GISAXS for in-situ and in-operando studies during thin film formation and processing. It has been shown that GISAXS presents unique capabilities as a noninvasive technique with intrinsic statistical relevance and time resolutions down to the millisecond regime. Moreover, GISAXS constitutes a very versatile technique that can be applied to a large variety of materials with a vast range of applications, and the relative easiness of combining it with other characterization

techniques for simultaneous measurements offers the possibility of correlating the film structure to its properties, of utmost importance in most of the applications of thin films.

In the near future, the present developments for the next generation of 2D X-ray photon counting pixel detectors will allow investigating even faster processes since frame rates higher than 10 kHz with large detector dynamic ranges are foreseen. Additionally, the application of present technique improvements to in-situ studies will further contribute to gain deeper knowledge of thin film fabrication and processing. In this sense, the present advances in grazing incidence resonant soft X-ray scattering (GI-RSoXS), with its inherent material contrast through tuning the incident beam energy to one of the absorption edges of the materials under investigation, will certainly help in understanding, e.g., alloying, blending or phase segregation phenomena in-situ with adequate time resolution. Furthermore, the decrease in beam emittance at synchrotrons is currently enabling longer sample to detector distances—up to several tens of meters—which translates in access to lower q ranges (of the order of 0.001 nm^{-1} or even lower, i.e., real space sizes in the micron range) by performing grazing incidence ultra-small angle X-ray scattering (GIUSAXS) experiments. Thus, through the combination of in-situ GIWAXS ($q \approx 1\text{--}50 \text{ nm}^{-1}$), GISAXS ($q \approx 0.01\text{--}1 \text{ nm}^{-1}$) and GIUSAXS ($q \approx 0.01\text{--}0.0001 \text{ nm}^{-1}$) real space structures from 1 \AA to $10 \text{ }\mu\text{m}$ will be accessible, which will provide a complete morphological description of the processes from the atomic structure to the microscopic regime allowing to establish an extremely important link between atomic, nanoscopic and macroscopic ordering, which is not yet fully developed.

Finally, the development of new magnet arrays in storage rings is currently taking place and diffraction-limited sources are not far from becoming available. This will provide an enhanced coherence of the X-ray beams and therefore, it is not difficult to anticipate a growth in the application of time-resolved coherent GISAXS (Co-GISAXS). So far, most of the GISAXS experiments are noncoherent, thus the scattered photon phase is lost making modeling indispensable during data analysis. On the contrary, in Co-GISAXS the phase information can be directly retrieved via mathematical algorithms so that, to some extent, the morphology of the scattering entity can be directly reconstructed from the experimental data. Furthermore, as already known from other X-ray coherent techniques such as X-ray photon correlation spectroscopy (XPCS), not only kinetics but also dynamics of the nano-objects may be probed. However, a good resolution of the speckles is necessary to guarantee an accurate determination of the dynamical processes. This requires a high q resolution that corresponds to small detector pixel size and for fast dynamic processes 2D X-ray photon counting pixel detectors with pixel sizes comparable to those of CCD detectors will be indispensable.

Acknowledgements

We would like to kindly acknowledge José Ángel Martín-Gago for the critical reading of the chapter as well as Stefan Kowarik for his valuable suggestions in Section 3.2. S.Y. acknowledges the financial support from the Knut and Alice Wallenberg Foundation.

Author details

Gonzalo Santoro^{1*} and Shun Yu²

*Address all correspondence to: gonzalo.santoro@icmm.es

¹ Materials Science Institute of Madrid (ICMM-CSIC), Madrid, Spain

² KTH Royal Institute of Technology, Stockholm, Sweden

References

- [1] Zhao XY, Wei CM, Yang L, et al. Quantum confinement and electronic properties of silicon nanowires. *Phys. Rev. Lett.* 2004; 92. DOI: 10.1103/PhysRevLett.92.236805.
- [2] Sun YG, Mayers B, Xia YN. Metal nanostructures with hollow interiors. *Adv. Mater.* 2003; 15:641–646. DOI: 10.1002/adma.200301639.
- [3] Narayanan R, El-Sayed MA. Shape-dependent catalytic activity of platinum nanoparticles in colloidal solution. *Nano Lett.* 2004; 4:1343–1348. DOI: 10.1021/nl0495256.
- [4] Kelly KL, Coronado E, Zhao LL, et al. The optical properties of metal nanoparticles: the influence of size, shape, and dielectric environment. *J. Phys. Chem. B.* 2003; 107:668–677. DOI: 10.1021/jp026731y.
- [5] Daniel MC, Astruc D. Gold nanoparticles: assembly, supramolecular chemistry, quantum-size-related properties, and applications toward biology, catalysis, and nanotechnology. *Chem. Rev.* 2004; 104:293–346. DOI: 10.1021/cr030698+.
- [6] Hentschel M, Saliba M, Vogelgesang R, et al. Transition from isolated to collective modes in plasmonic oligomers. *Nano Lett.* 2010; 10:2721–2726. DOI: 10.1021/nl101938p.
- [7] Jiao F, Frei H. Nanostructured cobalt oxide clusters in mesoporous silica as efficient oxygen-evolving catalysts. *Angew. Chem. Int. Ed.* 2009; 48:1841–1844. DOI: 10.1002/anie.200805534.
- [8] Ellison CJ, Torkelson JM. The distribution of glass-transition temperatures in nanoscopically confined glass formers. *Nat. Mater.* 2003; 2:695–700. DOI: 10.1038/nmat980.
- [9] Glatter O, Kratky O, editors. *Small Angle X-ray Scattering*. London: Academic Press Inc.; 1982. 515 p. ISBN: 0-12-286280-5.
- [10] Levine JR, Cohen LB, Chung YW, et al. Grazing-incidence small-angle X-ray-scattering – new tool for studying thin-film growth. *J. Appl. Crystallogr.* 1989; 22:528–532. DOI: 10.1107/s002188988900717x.

- [11] Müller-Buschbaum P. Grazing incidence small-angle X-ray scattering: an advanced scattering technique for the investigation of nanostructured polymer films. *Anal. Bioanal. Chem.* 2003; 376:3–10. DOI: 10.1007/s00216-003-1869-2.
- [12] Renaud G, Lazzari R, Leroy F. Probing surface and interface morphology with grazing incidence small angle X-ray scattering. *Surf. Sci. Rep.* 2009; 64:255–380. DOI: 10.1016/j.surfrep.2009.07.002.
- [13] Müller-Buschbaum P. A basic introduction to grazing incidence small-angle X-ray scattering. In: Ezquerro TA, Nogales A, García-Gutiérrez MC, et al., editors. *Applications of Synchrotron Light to Scattering and Diffraction in Materials and Life Sciences*. Berlin, Heidelberg: Springer; 2009. p. 61–89. DOI: 10.1007/978-3-540-95968-7_3.
- [14] Yoneda Y. Anomalous surface reflection of X rays. *Phys. Rev.* 1963; 131:2010–2013. DOI: 10.1103/PhysRev.131.2010.
- [15] Lu XH, Yager KG, Johnston D, et al. Grazing-incidence transmission X-ray scattering: surface scattering in the Born approximation. *J. Appl. Crystallogr.* 2013; 46:165–172. DOI: 10.1107/s0021889812047887.
- [16] Dosch H. Evanescent X-ray scattering. In: Dosch H, editor. *Critical Phenomena at Surfaces and Interfaces: Evanescent X-Ray and Neutron Scattering*. Berlin, Heidelberg: Springer; 1992. p. 6–31. DOI: 10.1007/BFb0045211.
- [17] Robinson IK, Tweet DJ. Surface X-ray diffraction. *Rep. Prog. Phys.* 1992; 55:599–651. DOI: 10.1088/0034-4885/55/5/002.
- [18] Lazzari R. IsGISAXS: a program for grazing-incidence small-angle X-ray scattering analysis of supported islands. *J. Appl. Crystallogr.* 2002; 35:406–421. DOI: 10.1107/s0021889802006088.
- [19] Babonneau D. FitGISAXS: software package for modelling and analysis of GISAXS data using IGOR Pro. *J. Appl. Crystallogr.* 2010; 43:929–936. DOI: 10.1107/s0021889810020352.
- [20] Chourou ST, Sarje A, Li XS, et al. HipGISAXS: a high-performance computing code for simulating grazing-incidence X-ray scattering data. *J. Appl. Crystallogr.* 2013; 46:1781–1795. DOI: 10.1107/s0021889813025843.
- [21] Durniak C, Ganeva M, Pospelov G, et al. BornAgain—software for simulating and fitting X-ray and neutron small-angle scattering at grazing incidence [Internet]. 2015. Available from: <http://www.bornagainproject.org> [Accessed: 2016-05-23].
- [22] Lee B, Yoon J, Oh W, et al. In-situ grazing incidence small-angle X-ray scattering studies on nanopore evolution in low-*k* organosilicate dielectric thin films. *Macromolecules.* 2005; 38:3395–3405. DOI: 10.1021/ma048214e.
- [23] Busch P, Rauscher M, Smilgies DM, et al. Grazing-incidence small-angle X-ray scattering from thin polymer films with lamellar structures—the scattering cross section in

- the distorted-wave Born approximation. *J. Appl. Crystallogr.* 2006; 39:433–442. DOI: 10.1107/s0021889806012337.
- [24] Salditt T, Metzger TH, Peisl J, et al. Determination of the height-height correlation function of rough surfaces from diffuse X-ray scattering. *Europhys. Lett.* 1995; 32:331. DOI: 10.1209/0295-5075/32/4/008.
- [25] Hexemer A, Mueller-Buschbaum P. Advanced grazing-incidence techniques for modern soft-matter materials analysis. *IUCrJ.* 2015; 2:106–125. DOI: 10.1107/s2052252514024178.
- [26] Lazzari R, Leroy F, Renaud G. Grazing-incidence small-angle X-ray scattering from dense packing of islands on surfaces: development of distorted wave Born approximation and correlation between particle sizes and spacing. *Phys. Rev. B.* 2007; 76. DOI: 10.1103/PhysRevB.76.125411.
- [27] Döhrmann R, Botta S, Buffet A, et al. A new highly automated sputter equipment for in situ investigation of deposition processes with synchrotron radiation. *Rev. Sci. Instrum.* 2013; 84. DOI: 10.1063/1.4798544.
- [28] Cantelli V, Geaymond O, Ulrich O, et al. The In situ growth of nanostructures on surfaces (INS) endstation of the ESRF BM32 beamline: a combined UHV-CVD and MBE reactor for in situ X-ray scattering investigations of growing nanoparticles and semiconductor nanowires. *J. Synchrotron Radiat.* 2015; 22:688–700. DOI: 10.1107/s1600577515001605.
- [29] Ibrahimkuty S, Seiler A, Prussmann T, et al. A portable ultrahigh-vacuum system for advanced synchrotron radiation studies of thin films and nanostructures: EuSi₂ nano-islands. *J. Synchrotron Radiat.* 2015; 22:91–98. DOI: 10.1107/s1600577514019705.
- [30] Renaud G, Lazzari R, Revenant C, et al. Real-time monitoring of growing nanoparticles. *Science.* 2003; 300:1416–1419. DOI: 10.1126/science.1082146.
- [31] Lazzari R, Renaud G, Revenant C, et al. Adhesion of growing nanoparticles at a glance: surface differential reflectivity spectroscopy and grazing incidence small angle X-ray scattering. *Phys. Rev. B.* 2009; 79:125428. DOI: 10.1103/PhysRevB.79.125428.
- [32] Revenant C, Renaud G, Lazzari R, et al. Defect-pinned nucleation, growth, and dynamic coalescence of Ag islands on MgO(001): an in situ grazing-incidence small-angle X-ray scattering study. *Phys. Rev. B.* 2009; 79:235424. DOI: 10.1103/PhysRevB.79.235424.
- [33] Kaune G, Metwalli E, Meier R, et al. Growth and morphology of sputtered aluminum thin films on P3HT surfaces. *ACS Appl. Mater. Interfaces.* 2011; 3:1055–1062. DOI: 10.1021/am101195m.
- [34] Schwartzkopf M, Buffet A, Korstgens V, et al. From atoms to layers: in situ gold cluster growth kinetics during sputter deposition. *Nanoscale.* 2013; 5:5053–5062. DOI: 10.1039/c3nr34216f.

- [35] Santoro G, Yu S, Schwartzkopf M, et al. Silver substrates for surface enhanced Raman scattering: correlation between nanostructure and Raman scattering enhancement. *Appl. Phys. Lett.* 2014; 104:243107. DOI: 10.1063/1.4884423.
- [36] Paul N, Metwalli E, Yao Y, et al. Templating growth of gold nanostructures with a CdSe quantum dot array. *Nanoscale.* 2015; 7:9703–9714. DOI: 10.1039/c5nr01121c.
- [37] Yu S, Santoro G, Sarkar K, et al. Formation of Al nanostructures on Alq3: an in situ grazing incidence small angle X-ray scattering study during radio frequency sputter deposition. *J. Phys. Chem. Lett.* 2013; 4:3170–3175. DOI: 10.1021/jz401585d.
- [38] Yu S, Santoro G, Yao Y, et al. Following the island growth in real time: Ag nanocluster layer on Alq3 thin film. *J. Phys. Chem. C.* 2015; 119:4406–4413. DOI: 10.1021/jp512675w.
- [39] Schwartzkopf M, Santoro G, Brett CJ, et al. Real-time monitoring of morphology and optical properties during sputter deposition for tailoring metal-polymer interfaces. *ACS Appl. Mater. Interfaces.* 2015; 7:13547–13556. DOI: 10.1021/acsami.5b02901.
- [40] Metwalli E, Körstgens V, Schlage K, et al. Cobalt nanoparticles growth on a block copolymer thin film: a time-resolved GISAXS study. *Langmuir.* 2013; 29:6331–6340. DOI: 10.1021/la400741b.
- [41] Erb DJ, Schlage K, Röhlberger R. Uniform metal nanostructures with long-range order via three-step hierarchical self-assembly. *Sci. Adv.* 2015; 1:e1500751. DOI: 10.1126/sciadv.1500751.
- [42] Roth SV, Santoro G, Risch JFH, et al. Patterned diblock co-polymer thin films as templates for advanced anisotropic metal nanostructures. *ACS Appl. Mater. Interfaces.* 2015; 7:12470–12477. DOI: 10.1021/am507727f.
- [43] Ritley KA, Krause B, Schreiber F, et al. A portable ultrahigh vacuum organic molecular beam deposition system for in situ X-ray diffraction measurements. *Rev. Sci. Instrum.* 2001; 72:1453–1457. DOI: 10.1063/1.1336822.
- [44] Ferrer P, Rubio-Zuazo J, Heyman C, et al. A multipurpose ultra-high vacuum-compatible chamber for in situ X-ray surface scattering studies over a wide range of temperature and pressure environment conditions. *J. Phys.: Conf. Series.* 2013; 425:132002. DOI: 10.1088/1742-6596/425/13/132002.
- [45] Schreiber F, Eberhardt A, Leung TYB, et al. Adsorption mechanisms, structures, and growth regimes of an archetypal self-assembling system: Decanethiol on Au(111). *Phys. Rev. B.* 1998; 57:12476–12481. DOI: 10.1103/PhysRevB.57.12476.
- [46] Kowarik S, Gerlach A, Sellner S, et al. Real-time observation of structural and orientational transitions during growth of organic thin films. *Phys. Rev. Lett.* 2006; 96:125504. DOI: 10.1103/PhysRevLett.96.125504.
- [47] Mayer AC, Kazimirov A, Malliaras GG. Dynamics of bimodal growth in pentacene thin films. *Phys. Rev. Lett.* 2006; 97. DOI: 10.1103/PhysRevLett.97.105503.

- [48] Kowarik S, Gerlach A, Schreiber F. Organic molecular beam deposition: fundamentals, growth dynamics, and in situ studies. *J. Phys.: Condens. Matter.* 2008; 20. DOI: 10.1088/0953-8984/20/18/184005.
- [49] Kowarik S, Gerlach A, Skoda MWA, et al. Real-time studies of thin film growth: measurement and analysis of X-ray growth oscillations beyond the anti-Bragg point. *Eur. Phys. J.: Special Topics.* 2009; 167:11–18. DOI: 10.1140/epjst/e2009-00930-y.
- [50] Woll AR, Desai TV, Engstrom JR. Quantitative modeling of in situ X-ray reflectivity during organic molecule thin film growth. *Phys. Rev. B.* 2011; 84. DOI: 10.1103/PhysRevB.84.075479.
- [51] Alvarez J, Lundgren E, Torrelles X, et al. Effect of a surfactant in homoepitaxial growth of Ag (001): dendritic versus faceted island morphologies. *Surf. Sci.* 2000; 464:165–175. DOI: 10.1016/S0039-6028(00)00648-8.
- [52] Fleet A, Dale D, Woll AR, et al. Multiple time scales in diffraction measurements of diffusive surface relaxation. *Phys. Rev. Lett.* 2006; 96. DOI: 10.1103/PhysRevLett.96.055508.
- [53] Ferguson JD, Arian G, Dale DS, et al. Measurements of surface diffusivity and coarsening during pulsed laser deposition. *Phys. Rev. Lett.* 2009; 103. DOI: 10.1103/PhysRevLett.103.256103.
- [54] Frank C, Banerjee R, Oettel M, et al. Analysis of island shape evolution from diffuse X-ray scattering of organic thin films and implications for growth. *Phys. Rev. B.* 2014; 90. DOI: 10.1103/PhysRevB.90.205401.
- [55] Bommel S, Kleppmann N, Weber C, et al. Unravelling the multilayer growth of the fullerene C₆₀ in real time. *Nat. Commun.* 2014; 5:5388. DOI: 10.1038/ncomms6388.
- [56] Frank C, Novak J, Banerjee R, et al. Island size evolution and molecular diffusion during growth of organic thin films followed by time-resolved specular and off-specular scattering. *Phys. Rev. B.* 2014; 90:045410. DOI: 10.1103/PhysRevB.90.045410.
- [57] Zykov A, Bommel S, Wolf C, et al. Diffusion and nucleation in multilayer growth of PTCDI-C8 studied with in situ X-ray growth oscillations and real-time small angle X-ray scattering. *J. Chem. Phys.* Accepted manuscript.
- [58] Vegso K, Siffalovic P, Jergel M, et al. A non-equilibrium transient phase revealed by in situ GISAXS tracking of the solvent-assisted nanoparticle self-assembly. *J. Nanopart. Res.* 2014; 16:1–11. DOI: 10.1007/s11051-014-2536-6.
- [59] Corricelli M, Altamura D, Curri ML, et al. GISAXS and GIWAXS study on self-assembling processes of nanoparticle based superlattices. *Cryst. Eng. Commun.* 2014; 16:9482–9492. DOI: 10.1039/C4CE01291G.
- [60] Chou KW, Yan B, Li R, et al. Spin-cast bulk heterojunction solar cells: a dynamical investigation. *Adv. Mater.* 2013; 25:1923–1929. DOI: 10.1002/adma.201203440.

- [61] Perlich J, Schwartzkopf M, Körstgens V, et al. Pattern formation of colloidal suspensions by dip-coating: an in situ grazing incidence X-ray scattering study. *Phys. Stat. Sol. Rapid Res. Lett.* 2012; 6:253–255. DOI: 10.1002/pssr.201206114.
- [62] Nagpure S, Das S, Garlapalli RK, et al. In situ GISAXS investigation of low-temperature aging in oriented surfactant-mesostructured titania thin films. *J. Phys. Chem. C.* 2015; 119:22970–22984. DOI: 10.1021/acs.jpcc.5b06945.
- [63] Smilgies D-M, Li R, Giri G, et al. Look fast: crystallization of conjugated molecules during solution shearing probed in-situ and in real time by X-ray scattering. *Phys. Stat. Sol. Rapid Res. Lett.* 2013; 7:177–179. DOI: 10.1002/pssr.201206507.
- [64] Abdellah A, Virdi KS, Meier R, et al. Successive spray deposition of P3HT/PCBM organic photoactive layers: material composition and device characteristics. *Adv. Funct. Mater.* 2012; 22:4078–4086. DOI: 10.1002/adfm.201200548.
- [65] Sarkar K, Braden EV, Pogorzalek S, et al. Monitoring structural dynamics of in situ spray-deposited zinc oxide films for application in dye-sensitized solar cells. *ChemSusChem.* 2014; 7:2140–2145. DOI: 10.1002/cssc.201402049.
- [66] Song L, Wang W, Körstgens V, et al. Spray Deposition of titania films with incorporated crystalline nanoparticles for all-solid-state dye-sensitized solar cells using P3HT. *Adv. Funct. Mater.* 2016; 26:1498–1506. DOI: 10.1002/adfm.201504498.
- [67] Herzog G, Benecke G, Buffet A, et al. In situ grazing incidence small-angle X-ray scattering investigation of polystyrene nanoparticle spray deposition onto silicon. *Langmuir.* 2013; 29:11260–11266. DOI: 10.1021/la402254q.
- [68] Zhang P, Santoro G, Yu S, et al. Manipulating the assembly of spray-deposited nanocolloids: in situ study and monolayer film preparation. *Langmuir.* 2016; 32:4251–4258. DOI: 10.1021/acs.langmuir.6b00892.
- [69] Palumbiny CM, Liu F, Russell TP, et al. The crystallization of PEDOT:PSS polymeric electrodes probed in situ during printing. *Adv. Mater.* 2015; 27:3391–3397. DOI: 10.1002/adma.201500315.
- [70] Pröller S, Liu F, Zhu C, et al. Following the morphology formation in situ in printed active layers for organic solar cells. *Adv. Energy Mater.* 2016; 6:1501580. DOI: 10.1002/aenm.201501580.
- [71] Moulin JF, Roth SV, Müller-Buschbaum P. Flow at interfaces: a new device for X-ray surface scattering investigations. *Rev. Sci. Instrum.* 2008; 79:015109. DOI: 10.1063/1.2816220.
- [72] Santoro G, Buffet A, Döhrmann R, et al. Use of intermediate focus for grazing incidence small and wide angle X-ray scattering experiments at the beamline P03 of PETRA III, DESY. *Rev. Sci. Instrum.* 2014; 85:043901. DOI: 10.1063/1.4869784.

- [73] Felici R, Jeutter NM, Mussi V, et al. In situ study of the dewetting behavior of Ni-films on oxidized Si(001) by GISAXS. *Surf. Sci.* 2007; 601:4526–4530. DOI: 10.1016/j.susc.2007.04.210.
- [74] Daudin R, Nogaret T, Schuelli TU, et al. Epitaxial orientation changes in a dewetting gold film on Si(111). *Phys. Rev. B.* 2012; 86. DOI: 10.1103/PhysRevB.86.094103.
- [75] Bommel S, Spranger H, Weber C, et al. Thermally-activated post-growth dewetting of fullerene C60 on mica. *Phys. Status Sol. Rapid Res. Lett.* 2015; 9:646–651. DOI: 10.1002/pssr.201510258.
- [76] Zhang J, Posselt D, Smilgies D-M, et al. Lamellar diblock copolymer thin films during solvent vapor annealing studied by GISAXS: different behavior of parallel and perpendicular lamellae. *Macromolecules.* 2014; 47:5711–5718. DOI: 10.1021/ma500633b.
- [77] Hejral U, Muller P, Balmes O, et al. Tracking the shape-dependent sintering of platinum-rhodium model catalysts under operando conditions. *Nat. Commun.* 2016; 7:10964. DOI: 10.1038/ncomms10964.
- [78] Ruge M, Golks F, Zegenhagen J, et al. In operando GISAXS studies of mound coarsening in electrochemical homoepitaxy. *Phys. Rev. Lett.* 2014; 112:055503. DOI: 10.1103/PhysRevLett.112.055503.
- [79] Modestino MA, Kusoglu A, Hexemer A, et al. Controlling nafion structure and properties via wetting interactions. *Macromolecules.* 2012; 45:4681–4688. DOI: 10.1021/ma300212f.
- [80] Wang W, Schaffer CJ, Song L, et al. In operando morphology investigation of inverted bulk heterojunction organic solar cells by GISAXS. *J. Mater. Chem. A.* 2015; 3:8324–8331. DOI: 10.1039/C5TA01109D.
- [81] Schaffer CJ, Palumbiny CM, Niedermeier MA, et al. Morphological degradation in low bandgap polymer solar cells—an in-operando study. *Adv. Energy Mater.* 2016; 1600712. DOI: 10.1002/aenm.201600712.
- [82] Daudin R, Revenant C, Davi G, et al. Growth and dewetting of gold on Si(1 1 1) investigated in situ by grazing incidence small angle X-ray scattering. *Physica E: Low Dimens. Syst. Nanostruct.* 2012; 44:1905–1909. DOI: 10.1016/j.physe.2012.05.021.
- [83] Bikondoa O, Carbone D, Chamard V, et al. Ageing dynamics of ion bombardment induced self-organization processes. *Sci. Rep.* 2013; 3:1850. DOI: 10.1038/srep01850.
- [84] Nugent KA. Coherent methods in the X-ray sciences. *Adv. Phys.* 2010; 59:1–99. DOI: 10.1080/00018730903270926.
- [85] Rebollar E, Vazquez de Aldana JR, Martin-Fabiani I, et al. Assessment of femtosecond laser induced periodic surface structures on polymer films. *Phys. Chem. Chem. Phys.* 2013; 15:11287–11298. DOI: 10.1039/c3cp51523k.

- [86] Martínez-Tong DE, Rodríguez-Rodríguez A, Nogales A, et al. Laser fabrication of polymer ferroelectric nanostructures for nonvolatile organic memory devices. *ACS Appl. Mater. Interfaces*. 2015; 7:19611–19618. DOI: 10.1021/acsami.5b05213.
- [87] Rebollar E, Rueda DR, Martín-Fabiani I, et al. In situ monitoring of laser-induced periodic surface sStructures formation on polymer films by grazing incidence small-angle X-ray scattering. *Langmuir*. 2015; 31:3973–3981. DOI: 10.1021/acs.langmuir.5b00285.
- [88] Körstgens V, Philipp M, Magerl D, et al. Following initial changes in nanoparticle films under laminar flow conditions with in situ GISAXS microfluidics. *RSC Adv*. 2014; 4:1476–1479. DOI: 10.1039/c3ra44554b.
- [89] Philipp M, Körstgens V, Magerl D, et al. Sorption of water and initial stages of swelling of thin PNIPAM films using in situ GISAXS microfluidics. *Langmuir*. 2015; 31:9619–9627. DOI: 10.1021/acs.langmuir.5b01978.
- [90] Schaffer CJ, Palumbiny CM, Niedermeier MA, et al. A direct evidence of morphological degradation on a nanometer scale in polymer solar cells. *Adv. Mater*. 2013; 25:6760–6764. DOI: 10.1002/adma.201302854.